ACS OMEGA

http://pubs.acs.org/journal/acsodf

Article

Geomechanics of Organic Matters Contained in Shales: A Molecular-Level Investigation

Elshad Aslanov, Saad Alafnan,* Mohamed Mahmoud, and Abdulazeez Abdulraheem

Cite This: *ACS Omega* 2022, 7, 31801−31812

Read Online

ACCESS | Metrics & More | Article Recommendations

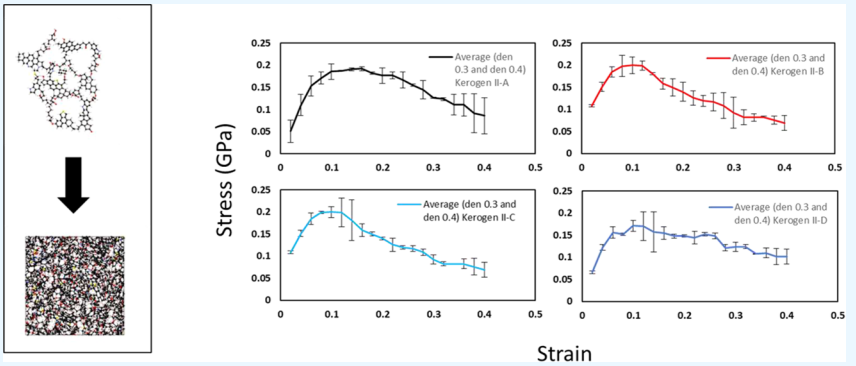

ABSTRACT: Petrophysical and mechanical properties of kerogen are difficult to obtain through conventional techniques due to length scale limitations. Characterization of kerogen requires the isolation of organic materials from the rock matrix, which is associated with a high probability of mechanical damage or chemical alteration of the properties. Alternatively, computational modeling and molecular representation of kerogens can be used to simulate the outcomes of the experimental work. Volumetric and thermodynamics modeling of kerogens has provided the means for recreating nanoscale structures virtually. This research implements existing three-dimensional (3D) kerogen macromolecules to form kerogen structures that can be analyzed for the mechanical behavior of type II organic matters, mainly found in shales, at different maturity levels. Additionally, the underlying factors that could control the mechanical behavior, such as the density and porosity, were investigated. The results are compared against those reported following a similar methodology or other advanced fine-scale experimental work. The results revealed an elastomer-like mechanical behavior of kerogen with comparable elastic moduli regardless of maturity level. Moreover, the mechanical behavior of kerogen was sensitive to the type of fluid contained within the structure. Such observations can help shed more light on the macroscopic mechanical properties of shales, especially for formations with high organic contents.

1. INTRODUCTION

The continuous decrease in the proven reserves of hydrocarbons trapped in conventional formations has given us the impetus to develop unconventional resources. The poor reservoir qualities of unconventional resources, such as low permeability and porosity, have been overcome by the advanced technologies of lateral drilling and hydraulic fracturing and other innovative techniques for enhanced recovery.[1,2] The term "unconventional" often refers to shaly formations, which comprise organic and inorganic constituents. Typical shale composition includes mostly clay, quartz, feldspar minerals, and a minor organic content. Hydraulic fracturing is the main stimulation technique applied during the completion of unconventional reservoirs. Therefore, a solid understanding of the formation's mechanical behavior is important to achieve the targeted design after treatment operations. Attributed to their heterogeneity and mineralogical complexity, determining the mechanical properties of shales is a challenging task. It requires individual assessment of each component and then modeling the behavior of the matrix as a whole. To investigate the effect of different shale components, Tan et al.[3] studied the formation from South China and Northern Australia. They found that elastic moduli correlated negatively with the presence of soft compounds such as clay, mica, and total organic content (TOC) but positively with harder ones such as feldspars and carbonates. Generally, in shales, increasing the content of quartz, pyrite, feldspar, and carbonates leads to an increase in elastic moduli. On the

Received: April 20, 2022
Accepted: August 22, 2022
Published: August 31, 2022

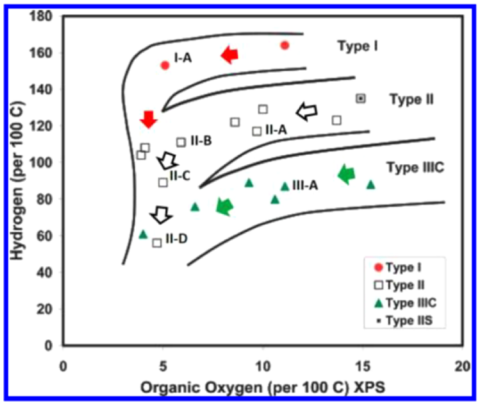

	C (%)	H (%)	O (%)
Type I	80	10.9	4.9
Type II	68.9	7.3	6.6
Type III	56.9	4.4	27.8

Figure 1. Van Krevelen type diagram reprinted with permission from [Ungerer, P.; Collell, J.; Yiannourakou, M. molecular modeling of the volumetric and thermodynamic properties of kerogen: influence of organic type and maturity. Energy and fuels 2015, 29 (1), 91−105.] Copyright [2015] [ACS energy and fuels].

contrary, a reverse trend is observed for increased contents of clay, mica, and organic matters.[3−5] Rybacki et al.[6] observed a similar trend in the elastic properties in European black shales. Hygroscopic characteristics of some clay minerals, which have a tendency to swell, lower the moduli of samples.[5] Ductile behavior is observed for formations with high contents in soft components.[6] Kerogen, among these components, is surrounded by a high degree of uncertainty due to their characteristically different nature and hence requires a detailed characterization. This paper concentrates on the study of kerogen's mechanical behavior by providing in-depth microscopic insights into different geomechanical aspects. The remainder of this research is organized as follows: the definition and the state-of-the-art modeling of kerogen mechanical properties are outlined in Section 1. This is followed by a detailed description of the molecular approach adopted in this work to construct kerogen structures and characterize their mechanical behavior. The results are then discussed, and conclusions are drawn.

1.1. Definition of Kerogen and Its Classification. Kerogen is a complex solid material that is composed of hydrocarbons. The chemical and physical properties of kerogens are a function of maturation and origin. The continuous process of maturation controls kerogen characteristics and can be linked to the type of hydrocarbons associated with them. Classification of organic materials (OMs) into the four main types according to their origin was first proposed by Durand and Espitalie.[7] Organic materials could be distinguished according to their depositional environment: land-derived (terrestrial) and aquatic. Alternatively, classifications of kerogens can be performed based on elemental analysis, such as hydrogen-to-carbon and oxygen-to-carbon ratios.[8] Typically, the Van Krevelen diagram shown in Figure 1 is used to classify kerogens and show how their elemental compositions change or evolve as they mature.

- Type I kerogen: highly aliphatic, with a H/C ratio greater than 1.5 and a low O/C content. This type of organic matter is associated with the lacustrine depositional environment.
- Type II kerogen: contains a large number of aromatics in comparison with Type I. Sulfur is always associated with this type of OM, either as pyrite or free sulfur. This type originated in a deep marine depositional environment. Type II comprises primarily planktons.
- Type III kerogen: derived from higher plant debris and frequently deposited in a shallow marine environment. They are considered hydrogen-poor and oxygen-rich organic materials.
- Type IV kerogen: hydrogen-poor and oxygen-rich. This organic matter is not always distinguished and is mostly combined with Type III.

1.2. Mechanical Properties of Kerogen through an Experimental Approach. As mentioned earlier, determining kerogen's mechanical properties is not an easy task due to its minimal content and fine dispersion in the rock structure. However, some methods allow for evaluating the mechanical parameters without isolation. There are two techniques in nanomechanics used to delineate the fine-scale heterogeneity of the mechanical behavior rather than relying only on average bulk properties: nanoindentation and atomic force microscopy (AFM). These methods can evince the contribution of individual phases, eliminating errors associated with nearby parts overlapping. The following properties can be calculated from these techniques: hardness and Young's, Bulk, and shear moduli. The experimental techniques reviewed in this paper are listed to provide information about existing methods and their limitations. However, experimental technologies are constantly evolving, and new innovative approaches are being developed.

Zeszotarski et al.[9] conducted a study on Type II kerogen from Woodford (USA) shale with a combined application of nanoindentation and atomic force microscopy. The hardness of organic matters was found to be greater than that of polymers, close to that of soft material such as gypsum, and lower than that of inorganic minerals. Later, Ahmadov et al.[10,11] studied in situ properties of organic-rich Bazhenov formation (Russia) by AFM, coupled with scanning electron microscopy (SEM) and confocal laser-scanning microscopy (CLSM). SEM images were used to identify kerogen regions, and then CLSM was implemented to confirm the existence of organic matters. Measurements confirmed that organic matters in the formation were softer than other minerals in the matrix. Kumar et al.[12] conducted similar tests on Woodford and Kimmeridge (USA) formations to determine the elastic properties of kerogen. The reported results were in good agreement with previous studies. Young's modulus values for Woodford shale varied in the range of 6−10 GPa. In fact, all aforementioned works followed similar methodologies with

https://doi.org/10.1021/acsomega.2c02474
ACS Omega 2022, 7, 31801−31812

minor changes in the resolution, which is due to the advancement of technologies. Eliyahu et al.[13] applied a recently developed PeakForce AFM mode to obtain the nanomechanical map of organic-rich samples. The obtained map showed the existence of distinct regions with different elastic properties. As expected, the elemental analysis revealed that the soft areas are carbon-rich, which corresponds to the organic materials. Table 1 summarizes the values of elastic properties obtained from the aforementioned publications.

Table 1. Comparison of Results from Different Studies

formation type	TOC (wt %)	V	E (GPa)	H (GPa)
Zeszotarski et al. (2004)				
Woodford shale (USA)	0.22	0.1	10.4	0.57
		0.2	10.1	
		0.3	9.6	
		0.4	8.8	
Ahmadov et al. (2011)				
Lockatong (USA)	2.84	0.07	13	n/a
		0.15	11.9	
		0.35	11	
		0.45	10.1	
Bazhenov (Russia)	0.03	0.02	5.9	n/a
		0.15	5.5	
		0.35	5.2	
		0.45	4.7	
Kumar et al. (2012)				
Woodford shale (USA)	0.13	0.3	6.2	0.2
Kimmeridge (USA)	0.49	0.3	5	0.2
Eliyahu et al. (2014)				
upper Jurassic source rock (USA)	0.5−4.50	0.3	0−25	n/a

The degree of maturation in unconventional resources determines the end products of the generation process and the final structure of kerogen. Valdes et al.[14] investigated the relationship between thermal maturity and elastic properties by extracting organic materials from the sample. The isolated matter was then synthetically heated to obtain structures of kerogen at different maturity levels. Elastic moduli of samples decreased at relatively lower temperatures (150 °C) and increased after a further increase in temperature. It was observed that the elastic moduli of the samples have a higher value at high maturity levels. This behavior was attributed to the graphitization of kerogen at higher temperatures and the increase in the cyclic moieties, which are more structurally stable compared to simple aliphatic ones. A similar tendency was observed in naturally mature shale (Young's modulus increase) in the Bakken formation.[15] It was explained by the reduction of organic content with increasing maturity. However, upon hydropyrolysis of the samples, elastic properties were found to follow a reverse trend. Heating of kerogen-derived bitumen generated at high temperatures, which is softer than organic matters, caused a reduction in the moduli. This can be interpreted from the highlighted literature that experimental analysis is associated with some degree of uncertainty. Heating the rock samples, for example, to induce maturation can alter other constituents of the matrix either mechanically or chemically, which in turn might influence the mechanical behavior. Hence, different factors, which are difficult to isolate, would contribute to the changes in the mechanical properties.

1.3. Mechanical Properties of Kerogen through a Modeling Approach. Kerogen isolation from the matrix for testing purposes introduces risks associated with the alteration of the original properties. This would limit the efficient characterization of such systems. Alternatively, computational modeling and molecular representation of kerogens can be used to mimic the outcomes of the experimental work. Since the 1960s, several analytical studies have been conducted to understand kerogen structures. Burlingame et al.[16] proposed the first kerogen model, although this model did not represent a full chemical structure of kerogen. The first detailed

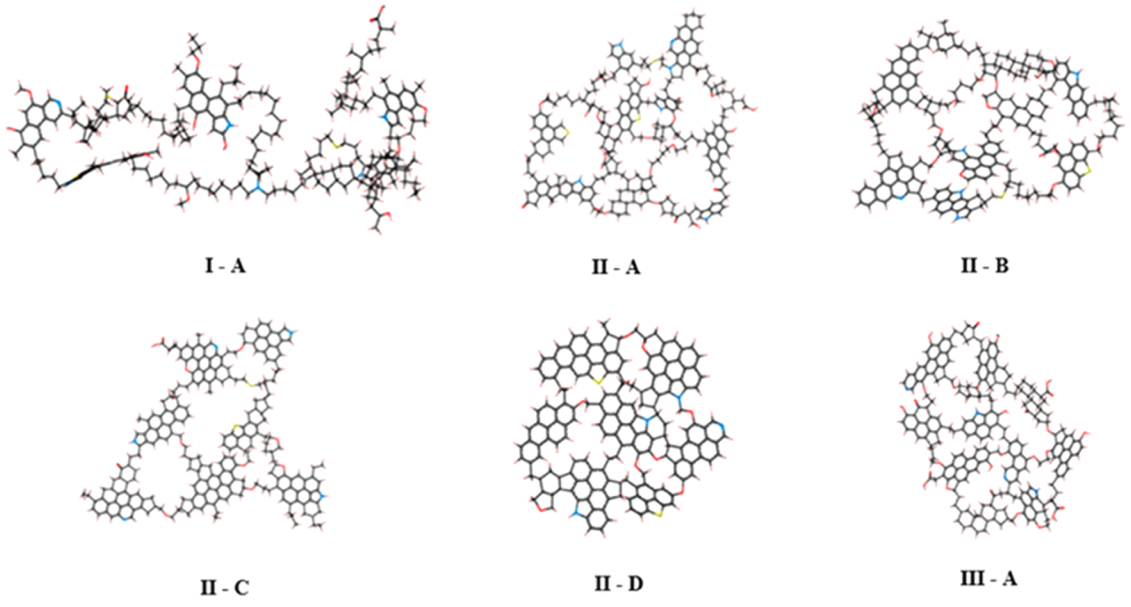

Figure 2. Prototypes of kerogen models utilized in the current study. Reprinted with permission from [Ungerer, P.; Collell, J.; Yiannourakou, M. molecular modeling of the volumetric and thermodynamic properties of kerogen: influence of organic type and Maturity. Energy and fuels 2015, 29 (1), 91−105.] Copyright [2015] [ACS Energy and fuels].

https://doi.org/10.1021/acsomega.2c02474
ACS Omega 2022, 7, 31801−31812

Table 2. Elemental Composition of Kerogen Models as Derived by Ungerer et al.[20]

###	I-A	II-A	II-B	II-C	II-D	III-A
composition	$C_{251}H_{385}O_{13}N_7S_3$	$C_{252}H_{294}O_{24}N_6S_3$	$C_{234}H_{263}O_{14}N_5S_2$	$C_{242}H_{219}O_{13}N_5S_2$	$C_{175}H_{102}O_9N_4S_2$	$C_{233}H_{204}O_{27}N_4$
H/C	1.53	1.17	1.12	0.905	0.58	0.886
O/C	0.052	0.095	0.06	0.054	0.051	0.116
N/C	0.028	0.024	0.022	0.021	0.023	0.017
S/C	0.012	0.012	0.009	0.006	0.011	

representation of kerogen has been described by Yen et al.[17] The published model was developed through studies of asphaltene structure. But this model was found to underestimate the typical density of organic materials. Later, Shiskin et al.[18] published a new model of Green River shale. Their model was successful in capturing various structural constituents in these oil shales compared to previous studies. One of the first applications of computers to the structural elucidation of moieties from sedimentary organic materials was published by Oka et al.[19] Because of the lack of computational power available at that time, such modeling was limited to low-molecular-weight compounds. The advancement in computational tools has allowed for the development of more representative three-dimensional (3D) structures. Ungerer et al.[20] generated six porotypes of kerogen structures (see Figure 2) at some range of maturity levels ranging from type I to type III.

Based on the available kerogen models, Zhang and Jamili[21] built a solid-state model of kerogen from the Green River formation to examine elastic properties and reported results (Young's modulus of 3.5 GPa, and Poisson's ratio of 0.25) that were close to those of previous studies conducted on the same formation by Yan and Han.[22] Kashinath et al.[23] carried out a similar study and reported outcomes within a close range. Values of Poisson's ratio were in line with experimentally obtained results and varied between 0.2 and 0.35.[11−13,24]

Molecular simulation approaches have been widely adopted in material science applications. The literature includes similar studies on silica, graphene-polythiophene, carbon nanotubes, and nanofibers.[25−28] A number of foregoing examples may be extended further; however, the main target was to show the applicability of the atomistic approach.

In this study, we aim to provide further extended analyses on kerogen type II that is present in shales. The four prototypes of kerogen II derived by Ungerer et al.[20] are utilized for this purpose. Different factors such as the density, porosity, and fluid type are to be considered. Both elastic and plastic regimes are to be investigated. Table 2 illustrates the differences between these models.

2. METHODOLOGY

2.1. Principles of Molecular Dynamics Simulation. Molecular dynamics (MD) is a powerful tool used to study the properties of materials by tracking molecular movement and interactions at the atomistic levels. MD simulations are frequently utilized in material science to obtain different properties. They are used when experimental approaches are inaccessible or time-consuming. To run MD simulations, three major steps are typically followed (see Figure 3).

1. Create an initial state: It is necessary to define the particles' initial position inside a simulation box.
2. Define interaction potentials: To introduce the interaction potentials, available verified force fields are used. These force fields are mathematical expressions that describe the interactions between molecules.
3. Predict particle movement: After defining force fields, Newton's equations of motion are integrated to predict the movement trajectories of the particles.

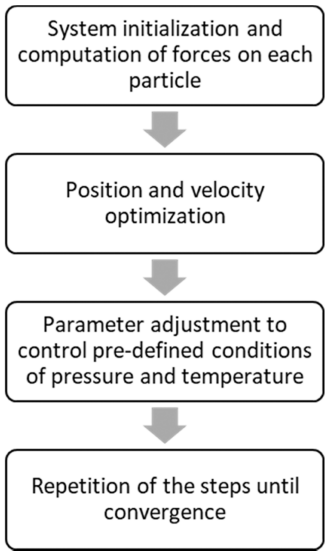

Figure 3. Typical flow of MD simulation (adopted in the current study).

While repeating these steps, the trajectory of each particle in the system is tracked during the simulation. Based on this, one could infer how the whole system behaves under specific controlled conditions of temperature and pressure.

2.2. Building Kerogen Models. All necessary procedures were performed using MedeA environment, including molecular dynamics (MD) modeling (MedeA LAMMPS). The polymer consistent forcefield plus (PCFF+) was selected to simulate atomic interaction during MD simulations, which has shown prominent performance in past studies.[20,29−34] The individual kerogen units were parameterized by the PCFF+ forcefield with the molecular interactions between two force centers i and j being described by 6−9 Lennard−Jones with the electrostatic potential term[35]

$$U_{LJ} = \epsilon\left[2\left(\frac{\sigma}{r_{ij}}\right)^9 - 3\left(\frac{\sigma}{r_{ij}}\right)^6\right] + \frac{q_i q_j}{4\pi\epsilon_0 r_{ij}} \quad (1)$$

$$\sigma = \left(\frac{\sigma_i^6 + \sigma_j^6}{2}\right)^{1/6} \quad (2)$$

$$\epsilon = 2\sqrt{\epsilon_i \epsilon_j}\,\frac{\sigma_i^3 \sigma_j^3}{\sigma_i^6 + \sigma_j^6} \quad (3)$$

https://doi.org/10.1021/acsomega.2c02474
ACS Omega 2022, 7, 31801−31812

where r_{ij} is the separation distance between the two force centers of charges q_i and q_j, ϵ_0 is the dielectric constant, σ is the distance at which the interaction potential between the two force centers is zero, and ϵ is the maximum amplitude of the potential well. σ and ϵ are both approximated using the sixth power combination rule as given by eqs 2 and 3.[35]

In the initial stage, kerogen units of type II, as introduced by Ungerer et al.,[20] were placed in the simulation box for each maturity level (II-A, II-B, II-C, and II-D). A number of kerogen units were placed in a periodic boundary box (i.e., 8−12 units). The density of the cubic cell before running the simulation was set to 0.2 g/cm^3. This step was done to eliminate instability issues that may arise in the subsequent simulation steps. After building the simulation box, an isochoric−isothermal *NVT* simulation at 900 K for 250 ps was performed. *NVT* is the constant volume and temperature molecular dynamics in which the amount of matter (N), volume (V), and temperature (T) are kept constant with the Nose−Hoover thermostat (in our case). The simulation was started at a high temperature as recommended by the original developers of the kerogen units to speed up the relaxation time.[20] This high temperature does not impact the integrity of the structure as the selected forcefield does not allow for breaking and forming bonds. Then, the structure was relaxed through four consecutive isobaric−isothermal NPT stages by decreasing the temperature from 900 to 350 K at a constant pressure of 20 MPa with a timestep of 1 fs (i.e., 350 K and 20 MPa are deemed to be representative of typical reservoir conditions). The aforementioned procedures were repeated four times for each kerogen prototype to generate sufficient statistics. Figure 4 summarizes all of the described steps followed in the construction phase of kerogen.

2.3. Mechanical Properties from the Elastic Theory.

The mechanical parameters of a structure can be found by deforming Bravais lattice vectors of the unit structure by applying strain. The created distortion produces changes in the total energy of the system.[36,37] Mathematically, this process can be expressed as

$$U_1 = \frac{E_t - E_0}{V_0} = \frac{1}{2}\sum_{i=1}^{6}\sum_{j=1}^{6} C_{ij}e_i e_j \tag{4}$$

where U is the total energy change during the distortion process, E_0 and E_t are energies before and after distortion, respectively, V_0 is the original volume of the unit cell, e_i and e_j are components of the strain matrix, and C is the Voigt stiffness matrix, which comprises 36 elements and can be represented as

$$C = \begin{bmatrix} c_{11} & c_{12} & c_{13} & c_{14} & c_{15} & c_{16} \\ c_{21} & c_{22} & c_{23} & c_{24} & c_{25} & c_{26} \\ c_{31} & c_{32} & c_{33} & c_{34} & c_{35} & c_{36} \\ c_{41} & c_{42} & c_{43} & c_{44} & c_{45} & c_{46} \\ c_{51} & c_{52} & c_{53} & c_{54} & c_{55} & c_{56} \\ c_{61} & c_{62} & c_{63} & c_{64} & c_{65} & c_{66} \end{bmatrix}$$

However, it is possible to reduce the matrix to a simpler form. The number of unknown elements depends on the symmetry of the structure. Table 3 summarizes the number of linearly independent elements for different symmetries.

Table 3. Number of Independent Elements in the Stiffness Matrix Depending on the Symmetry Type

symmetry Type	independent elements in matrix
cubic	3
hexagonal	5
orthorhombic	9
monoclinic	13
triclinic	21

Kerogen models analyzed in our study were initially placed in a cubic simulation box; therefore, the stiffness matrix is anticipated to have a cubic symmetry. Consequently, the number of independent elements reduces to 3, and the matrix can be written as follows

$$C = \begin{bmatrix} c_{11} & c_{12} & c_{12} & 0 & 0 & 0 \\ c_{12} & c_{11} & c_{12} & 0 & 0 & 0 \\ c_{12} & c_{12} & c_{11} & 0 & 0 & 0 \\ 0 & 0 & 0 & c_{44} & 0 & 0 \\ 0 & 0 & 0 & 0 & c_{44} & 0 \\ 0 & 0 & 0 & 0 & 0 & c_{44} \end{bmatrix}$$

The steps followed to find unknown elements C_{11}, C_{12}, and C_{44} are given below.[38]

STEP 1

The strain array is defined as $e = (0, 0, 0, \delta, \delta, \delta)$, where δ is the strain value. This step allows for a unique determination of C_{44}. As a result, eq 4 becomes

$$U_2 = \frac{3}{2}C_{44}\delta^2 \rightarrow C_{44} = \frac{2U}{3\delta^2} \tag{5}$$

STEP 2

The strain array is defined as $e = (\delta, \delta, 0, 0, 0, 0)$, where δ is the strain value. This step reduces eq 4 to the following form

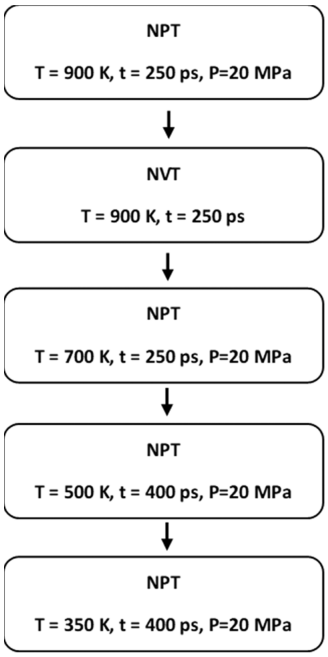

Figure 4. *NVT*/*NPT* simulation flowchart to build representative kerogen models.

https://doi.org/10.1021/acsomega.2c02474
ACS Omega 2022, 7, 31801−31812

$$U_3 = (C_{11} + C_{12})\delta^2 \quad (6)$$

STEP 3

The strain array is defined as $e = (\delta, \delta, \delta, 0, 0, 0)$, where δ is the strain value. This step reduces eq 4 as follows

$$U = \frac{3}{2}(C_{11} + C_{12})\delta^2 \quad (7)$$

By solving eqs 6 and 7 simultaneously, C_{11} and C_{12} can be quantified.

Mechanical properties of the kerogen structure can be calculated from the single-crystal data by following the Voigt−Reuss−Hill method.[39] This method predicts lower (G_R) and upper (G_V) bounds. Based on the Voigt−Reuss−Hill method, for the cubic lattice, shear modulus (G), bulk modulus (K), Young's modulus (E), and Poisson's ratio (ν) can be determined as follows

$$G_R = \frac{5C_{44}(C_{11} - C_{12})}{4C_{44} + 3(C_{11} - C_{12})} \quad (8)$$

$$G_V = \frac{C_{11} - C_{12} + 3C_{44}}{5} \quad (9)$$

$$G = \frac{G_R + G_V}{2} \quad (10)$$

$$K = \frac{C_{11} + 2C_{12}}{3} \quad (11)$$

$$E = \frac{9KG}{3K + G} \quad (12)$$

$$\nu = \frac{3K - 2G}{2(3K + G)} \quad (13)$$

Kerogen structures were subjected to strain starting from 0.02 to 0.4 with an increase of 0.02 to obtain the stress−strain relationship. After obtaining stress−strain curves, the appropriate strain values from the elastic region are used to calculate the elastic constants.

2.4. Void Space Calculation. Void spaces in the structure can be found by inserting nonoverlapping spheres at the vertices of the resulting polyhedral grid with a predefined threshold size.[40] In this study, an algorithm was used to insert the spheres into the available spaces inside the kerogen unit with the minimum radius selected as 0.2 nm. After obtaining all inserted spheres, the total pore volume (V_p) was determined by calculating each sphere's volume and adding them up. The bulk volume (V_b) was computed using lattice dimensions (a, b, c) of the kerogen units. The porosity (φ) was calculated using a ratio of total void space in the structure to the structure's bulk volume.

$$V_p = \sum_{i=1}^{n} \frac{4}{3}\pi r_i^3 \quad (14)$$

$$V_b = a \times b \times c \quad (15)$$

$$\varphi = \frac{V_p}{V_b} \quad (16)$$

3. RESULTS AND DISCUSSION

3.1. Density and Porosity of Kerogens. As detailed in the methodology section, kerogen structures were built starting from less dense structures and running the stated MD protocol. Different independent configurations for each kerogen type were obtained to assess the robustness of the followed approach and its reproducibility. After the MD simulations, the densities of kerogen structures were found to be in the range of 1.11−1.29. These values were in good agreement with those of previous studies conducted on an experimental and computational basis.[20,41] The calculated porosities of the kerogens were between 0.13 and 0.15, and the highest corresponded to the most mature one (II-D).

It should be pointed out that there was no clear relationship between maturity level and density. The same conclusion can be drawn for the maturity−porosity relation. Nevertheless, the most mature kerogen was found to have the highest density and porosity. Table 4 shows the density and porosity of each configuration. For brevity and clarity of information in the coming sections, the densities and porosities for each kerogen type were averaged considering all configurations generated for each type. This step should not introduce errors as the porosity and density of most configurations are within a close range.

Table 4. Density and Porosity Values for Kerogen Type II at Different Maturity Levels

kerogen type	configuration	density (g/cm^3)	ϕ
II-A	1	1.13	0.141
	2	1.12	0.142
	3	1.13	0.130
	4	1.13	0.141
II-B	1	1.10	0.139
	2	1.11	0.146
	3	1.12	0.153
	4	1.11	0.152
II-C	1	1.17	0.142
	2	1.19	0.134
	3	1.17	0.150
	4	1.16	0.153
II-D	1	1.28	0.152
	2	1.29	0.140
	3	1.24	0.147
	4	1.26	0.156

3.2. Deformation of Kerogens. The kerogen's stress−strain behavior was created by applying strain from 0.02 to 0.4 with an increase of 0.02 (see Figure 5). Generally, different structures followed the same trend in all cases with slight deviations. The elastic region for all kerogen types fell in a strain range of 0.04−0.15. The stress−strain relationship for all types had similar trends suggesting that the thermal maturity did not significantly impact the mechanical properties.

3.3. Mechanical Properties of Kerogens. Mechanical properties of kerogen were determined after applying strain within the elastic interval of the stress−strain curve. Table 5 shows the results of simulations against the average values of density and porosity. The most mature kerogen type was observed to have the lowest moduli values compared to other types. On the contrary, type II-B was found to have the highest shear and Young's moduli. Poisson's ratio was in the range between 0.39 and 0.42, with the maximum and the minimum corresponding to type II-D and II-B, respectively. The

https://doi.org/10.1021/acsomega.2c02474
ACS Omega 2022, 7, 31801−31812

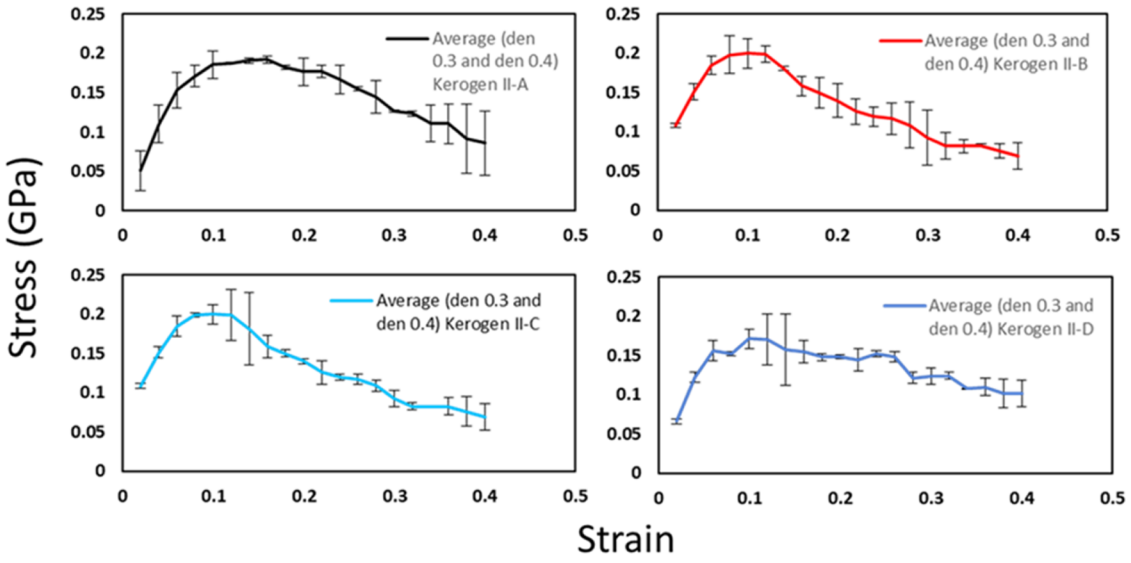

Figure 5. Stress−strain relationship of kerogens for two sets of configurations revealing similar behavior among all type II models.

Table 5. Mechanical Properties, Average Density, and Average Porosity Values of Kerogens

kerogen type	K (GPa)	G (GPa)	E (GPa)	Poisson's ratio	density (g/cm^3)	ϕ
II-A	3.71	0.79	2.20	0.401	1.13	0.138
II-B	3.57	0.87	2.42	0.386	1.11	0.147
II-C	3.62	0.81	2.27	0.395	1.18	0.144
II-D	3.39	0.60	1.70	0.418	1.26	0.149

deformation and mechanical constant analyses revealed an insignificant influence of thermal maturity on the mechanical behavior of kerogen, which is inconsistent with the reported experimental findings available in the literature where brittleness increases with maturation. This might be explained by the elastomeric behavior of kerogen, where the temperature has a pronounced effect on the mechanical properties. Experimental assessment of the mechanical behavior is usually carried out at ambient temperature, whereas the reported findings of this study were made at a higher temperature (i.e., 350 K was used as a typical reservoir condition). As the temperature increases, the elemental and structural differences become minimal. The deformation was repeated at the ambient temperature (see Figure 6), and it showed that the kerogen with the highest level of maturity exhibited a more brittle behavior, unlike the case of that at higher temperature (i.e., 350 K), where both kerogen models had a similar mechanical response as shown in Figure 7.

Moduli vs average densities were plotted, as given in Figure 8. Generally, no clear relationship between elastic moduli and density was observed. Coefficients of determination indicated a weak correlation between moduli and density. The same plot was generated between porosity and mechanical properties (see Figure 9). A slight decreasing trend of the moduli was observed.

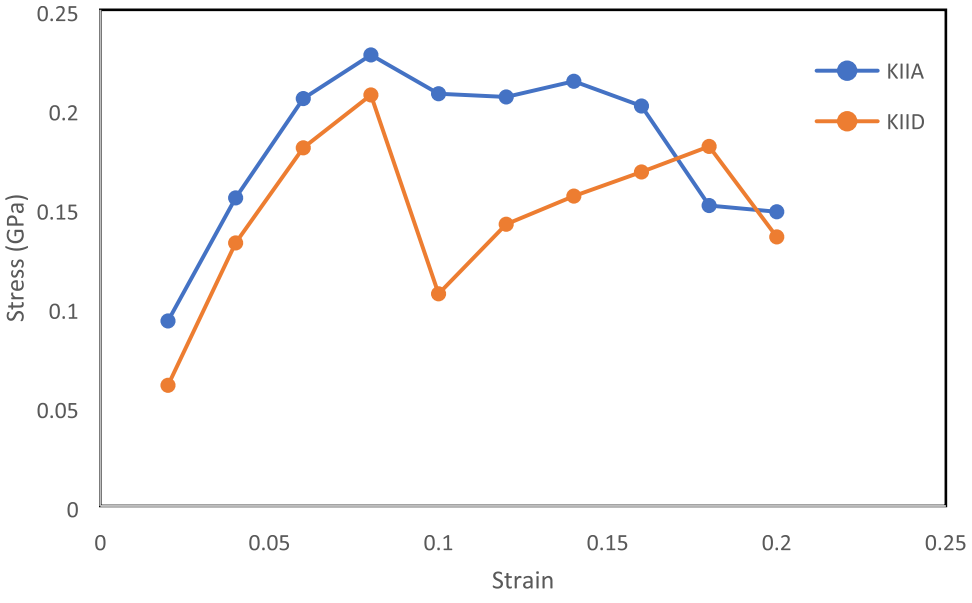

Figure 6. Stress−strain relationship of kerogen II-A and II-D at 300 K.

https://doi.org/10.1021/acsomega.2c02474
ACS Omega 2022, 7, 31801−31812

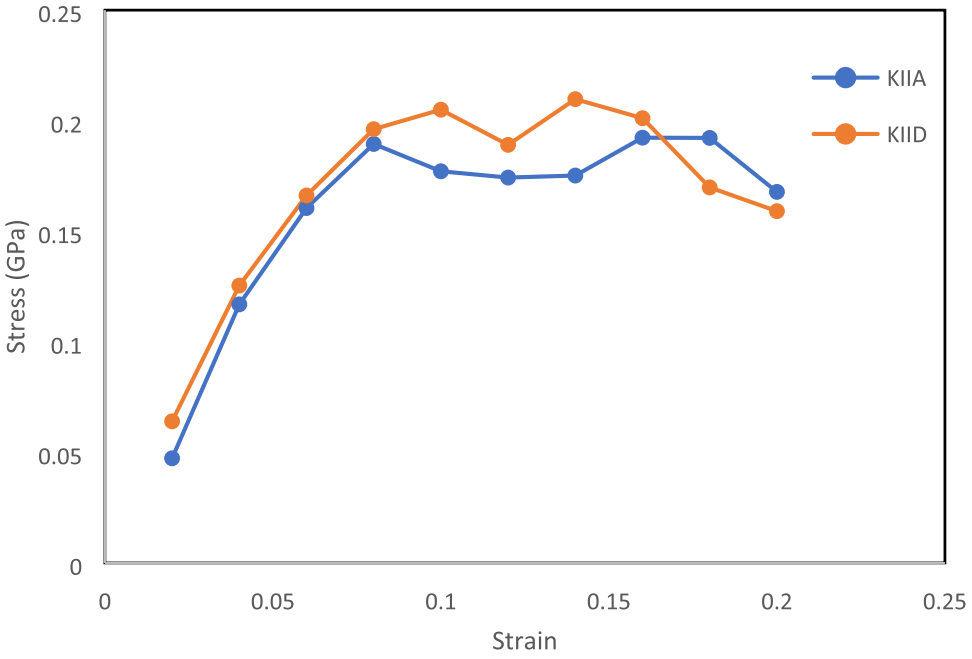

Figure 7. Stress−strain relationship of kerogen II-A and II-D at 350 K.

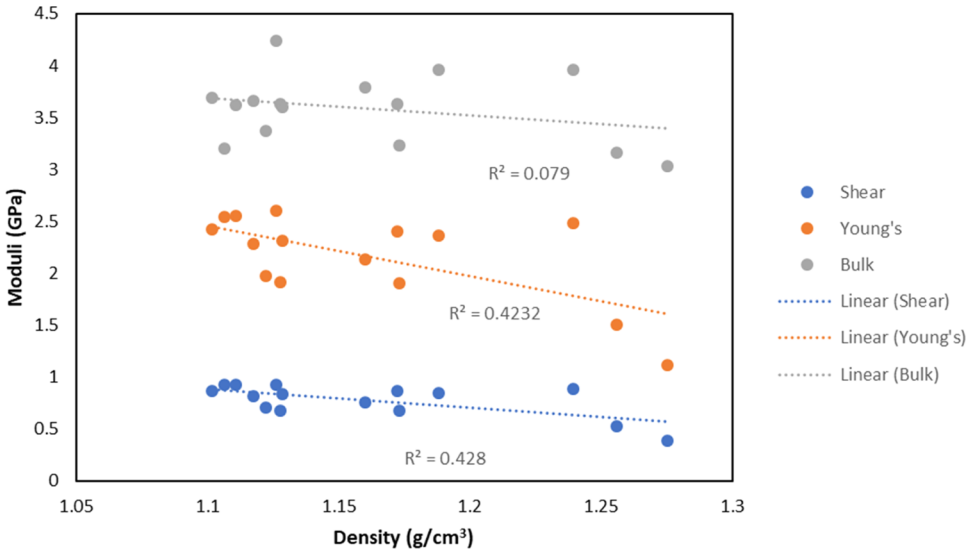

Figure 8. Relationship between density and different moduli values of kerogens.

The previously presented structures were constructed from their respective units following the molecular dynamics approach detailed in Section 2.2. The porosity obtained in all cases is attributed to the intermolecular spaces between macromolecular units. Porosity values, as reported in Table 4, were in a narrow range such that no clear correlation between porosity and mechanical properties could be observed. In reality, however, pressure buildup during catagenesis can induce micropores, which in turn increases the porosity and alters the mechanical behavior.[42−44] Thermal maturation may also influence the overall mechanical state of the formation through the induced microcracks, which could penetrate the inorganic minerals. This might explain the more pronounced, experimentally observed differences in the mechanical behavior of shales at different maturation levels.

3.4. Correlation of Mechanical Properties with Porosity. To further delineate the impact of porosity on the mechanical properties, porosity-controlled kerogen structures were generated following the previously outlined molecular dynamics construction protocol. To control the porosity, a specified number of director molecules were inserted in the initialization stage and then removed upon final convergence to the targeted pressure and temperature (i.e., heptane was used as the choice of director in our case). The same approach of using heptane to control the porosity was followed in some other articles.[29,32] The broader range of porosity can help establish a better understanding of how mechanical properties vary with porosity. The created structures, which consisted of kerogen II-A, had porosity values of 14.33, 14.96, 17.65, and 20.25%, respectively. The results revealed a strong correlation with porosity where all of the mechanical constants had a negative relationship with porosity, as shown in Figure 10.

3.5. Type of Fluid. Kerogens, under subsurface conditions, can be saturated with natural gas. The gas contained in the

https://doi.org/10.1021/acsomega.2c02474
ACS Omega 2022, 7, 31801−31812

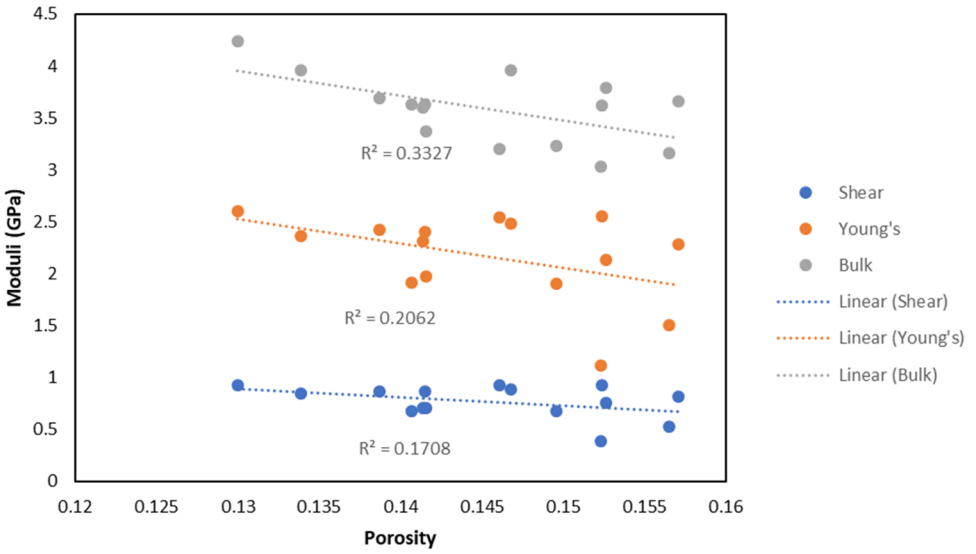

Figure 9. Relationship between porosity and different moduli values of kerogens.

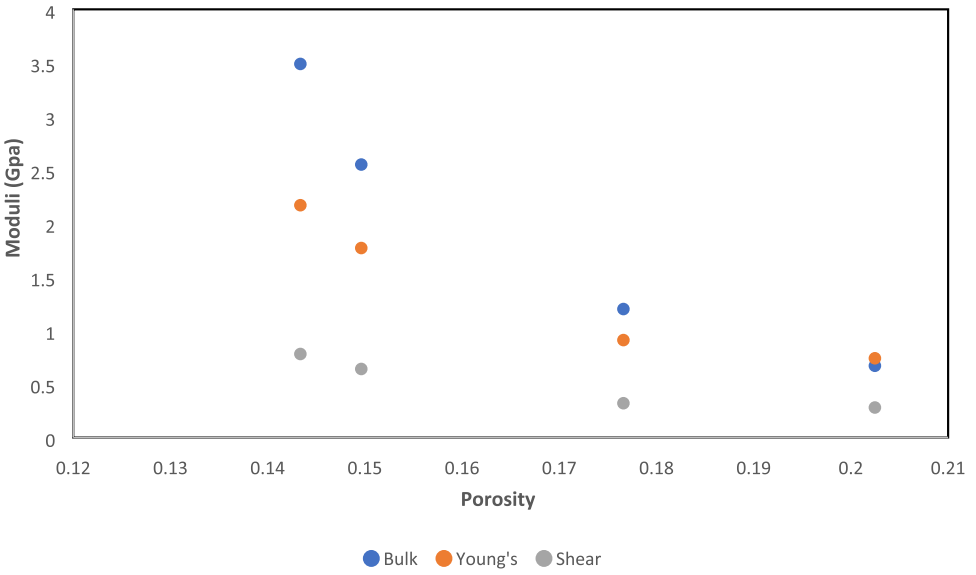

Figure 10. Moduli vs porosity for the porosity-controlled structure consisting of kerogen II-A as the building block unit.

organic materials of shales primarily consists of methane with smaller fractions of other light and intermediate hydrocarbons. Carbon dioxide can also exist either naturally or injected for sequestration or hydraulic fracturing purposes.[45] In this section, the impact of fluid type is investigated. Kerogen II-D is subjected to adsorption considering two cases of pure methane and pure carbon dioxide. Gibbs ensemble Monte Carlo simulation of the methane−kerogen and carbon dioxide−kerogen interactions can be interpreted as the amount of gas phase. The sorption calculations were carried out at 350 K and 41.34 MPa, which are representative of the typical initial conditions encountered in reservoirs. At these conditions, the Peng−Robinson equation of state was used to approximate the fugacity of methane and carbon dioxide. The fugacity of methane was 35.84 MPa, while that of carbon dioxide was 31.18 MPa. The selected kerogen II-D hosted 58 molecules of methane and 78 molecules of carbon dioxide at the specified conditions of temperature and pressure. The saturated structures with methane and carbon dioxide were analyzed for the mechanical behavior following the previously outlined molecular calculations.

The mechanical tensile test revealed sensitivity to the presence of fluid (see Figure 11), where the stress−strain curve shifted downward, suggesting a slight reduction in the yield strength. Interestingly, the stress−strain shift was more pronounced in the case of methane.

The elastic moduli were then calculated, as shown in Table 6. The bulk modulus showed an increase of 33 and 50% when the structure was saturated with methane and carbon dioxide, respectively. A similar trend was observed in Young's modulus, where the calculated values for methane and carbon dioxide were 8.5 and 22% higher, respectively. Shear modulus was associated with 7 and 20% increases for methane and carbon dioxide, respectively. The sensitivity of mechanical behavior to the fluid type might be attributed to the intermolecular interactions between adsorbent (kerogen) and adsorbate (methane or carbon dioxide), where Gibbs calculations revealed a lower electrostatic potential for the methane case than the carbon dioxide case (i.e., the magnitude of the grid

https://doi.org/10.1021/acsomega.2c02474
ACS Omega 2022, 7, 31801−31812

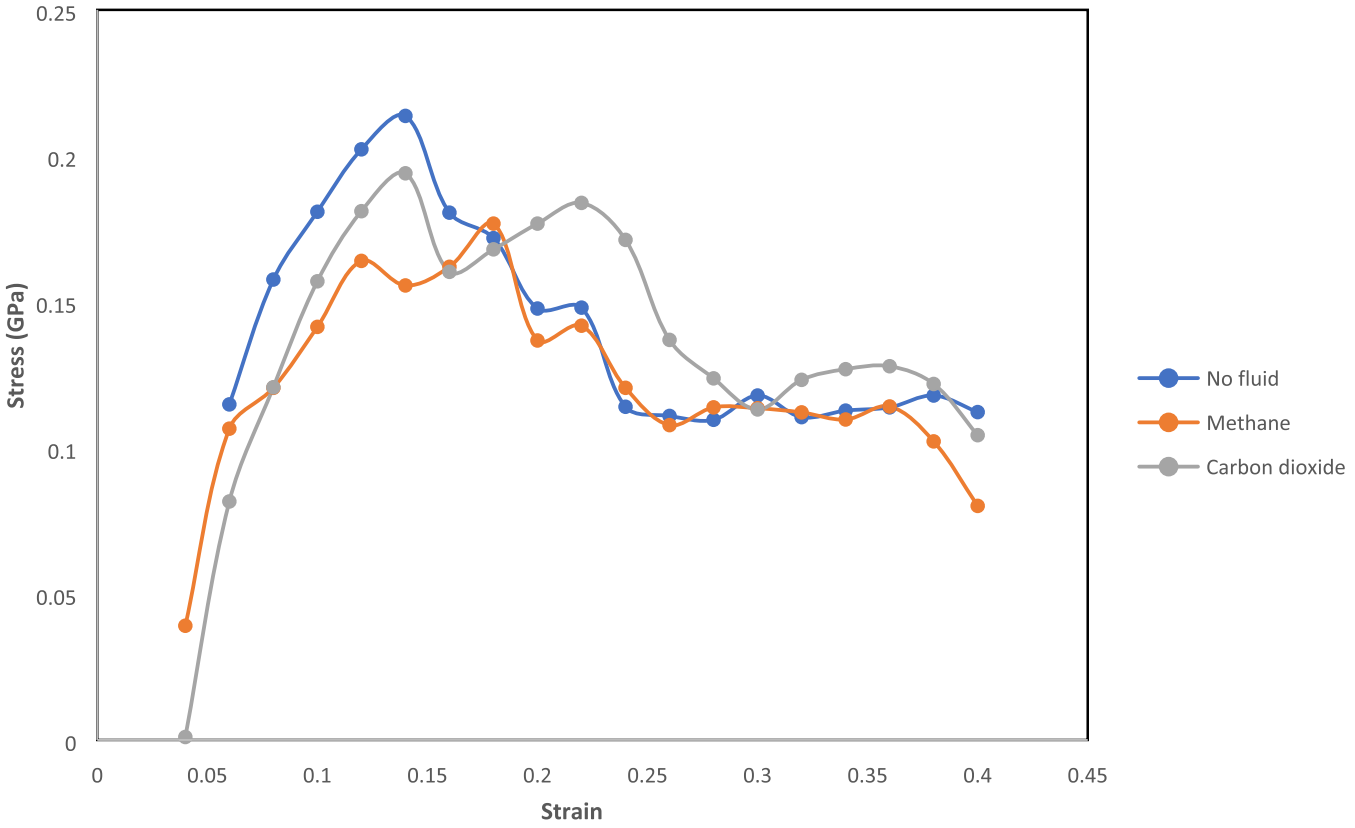

Figure 11. Stress–strain relationship of kerogen II-D for no fluid, methane, and carbon dioxide cases.

Table 6. Mechanical Properties of II-D Kerogen for No Fluid and When Saturated with Methane and Carbon Dioxide

property	no fluid	CH_4	CO_2
Bulk (GPa)	3.99	5.31	5.95
Shear (GPa)	0.88	0.94	1.06
Young's (GPa)	2.46	2.67	3.01
Poisson's ratio	0.3972	0.4167	0.4156

potential when saturated with methane was 17.001 kJ/mol, while it was 23.577 kJ/mol for carbon dioxide).

4. CONCLUSIONS

In this study, representative kerogen structures of type II were recreated to study the geomechanics of the organic materials present in shales. The outcomes of the performed analyses can be summarized as follows.

- Kerogen structures, regardless of thermal maturity, exhibited elastomer-like behavior, which is characteristically different from that of the other shale matrix constituents. Such behavior is anticipated to impact the macroscopic geomechanics of shales, especially for organic-rich formations and, consequently, the organic–inorganic interface. This occurrence is attributed to the plastic deformation of organic compounds under applied stress, leading to the closure of fractures.
- Thermal maturity was not found to influence the mechanical properties of kerogen significantly.
- Kerogen II-D, which was the most mature one, had the lowest elastic moduli, which might be explained by its relatively higher intermolecular porosity.
- Porosity can be formed as a result of pressure buildup during oil- and gas-generation windows. To investigate the impact of induced porosity on mechanical behavior, porosity-controlled structures were used. The results revealed a negative correlation between mechanical properties and porosity.
- The fluid contained within the kerogen structure was found to have an influence on mechanical behavior.
- Kerogen is a complex heterogeneous structure consisting of a range of macerals in different compositions. It is recommended that the approach followed in this study be extended to cover these nanoscale intricacies for a better understanding of the organic matters' mechanical properties.

AUTHOR INFORMATION

Corresponding Author

Saad Alafnan − *Department of Petroleum Engineering, King Fahd University of Petroleum and Minerals, Dhahran 31261, Saudi Arabia*; orcid.org/0000-0001-9124-8340; Email: safnan@kfupm.edu.sa

Authors

Elshad Aslanov − *Department of Petroleum Engineering, King Fahd University of Petroleum and Minerals, Dhahran 31261, Saudi Arabia*

Mohamed Mahmoud − *Department of Petroleum Engineering, King Fahd University of Petroleum and Minerals, Dhahran 31261, Saudi Arabia*; orcid.org/0000-0002-4395-9567

Abdulazeez Abdulraheem − *Department of Petroleum Engineering, King Fahd University of Petroleum and*

https://doi.org/10.1021/acsomega.2c02474
ACS Omega 2022, 7, 31801−31812

Minerals, Dhahran 31261, Saudi Arabia; orcid.org/0000-0002-9994-4436

Complete contact information is available at: https://pubs.acs.org/10.1021/acsomega.2c02474

Notes

The authors declare no competing financial interest.

The datasets used and/or analyzed during the current study are available from the corresponding author upon reasonable request.

The authors declare that they have no known competing financial interests or personal relationships that could have appeared to influence the work reported in this paper.

■ ACKNOWLEDGMENTS

The authors acknowledge the support provided by the College of Petroleum Engineering and Geosciences at King Fahd University of Petroleum and Minerals in Saudi Arabia for the subscription granting access to resource materials, journal articles reviewed in this work, and MedeA interface.

■ NOMENCLATURE

U	total energy change
E_0	energy before distortion
E_t	energy after distortion
V_0	initial volume
C	Voigt stiffness matrix
e	strain matrix
δ	strain value in the strain matrix
G_R	lower shear modulus limit
G_V	upper shear modulus limit
V_p	pore volume
V_b	bulk volume
r	radius
a, b, c	dimensions
φ	porosity
ν	Poisson's ratio
E	Young's modulus
G	shear modulus
K	bulk modulus

■ REFERENCES

(1) Alafnan, S.; Aljawad, M.; Alismail, F.; Almajed, A. Enhanced Recovery from Gas Condensate Reservoirs through Renewable Energy Sources. *Energy Fuels* **2019**, *33*, 10115−10122.

(2) Afagwu, C.; Abubakar, I.; Kalam, S.; Al-Afnan, S. F.; Awotunde, A. A. Pressure-Transient Analysis in Shale Gas Reservoirs: A Review. *J. Nat. Gas Sci. Eng.* **2020**, *78*, No. 103319.

(3) Tan, J.; Horsfield, B.; Fink, R.; Krooss, B.; Schulz, H. M.; Rybacki, E.; Zhang, J.; Boreham, C. J.; van Graas, G.; Tocher, B. A. Shale Gas Potential of the Major Marine Shale Formations in the Upper Yangtze Platform, South China, Part III: Mineralogical, Lithofacial, Petrophysical, and Rock Mechanical Properties. *Energy Fuels* **2014**, *28*, 2322−2342.

(4) Wanniarachchi, W. A. M.; Ranjith, P. G.; Perera, M. S. A.; Nguyen, J. T.; Rathnaweera, T. D. In *An Experimental Study to Investigate the Effect of Mineral Composition on Mechanical Properties of Shale Gas Formations*. 51st US Rock Mechanics/Geomechanics Symposium, 2017.

(5) Nandi, A.; Conde, R. Unconfined Compressive Strength of Shale As a Function of Petrophysical Properties: A Case Study From Eastern Tennessee. *J. Tenn. Acad. Sci.* **2011**, *86*, 56−62.

(6) Rybacki, E.; Reinicke, A.; Meier, T.; Makasi, M.; Dresen, G. What Controls the Mechanical Properties of Shale Rocks? - Part I: Strength and Young's Modulus. *J. Pet. Sci. Eng.* **2015**, *135*, 702−722.

(7) Durand, B.; Espitalié, J. Geochemical Studies on the Organic Matter from the Douala Basin (Cameroon)-II. Evolution of Kerogen. *Geochim. Cosmochim. Acta* **1976**, *40*, 801−808.

(8) Onishchenko, Y. V.; Vakhin, A. V.; Gareev, B. I.; Batalin, G. A.; Morozov, V. P.; Eskin, A. A. The Material Balance of Organic Matter of Domanic Shale Formation after Thermal Treatment. *Pet. Sci. Technol.* **2019**, *37*, 756−762.

(9) Zeszotarski, J. C.; Chromik, R. R.; Vinci, R. P.; Messmer, M. C.; Michels, R.; Larsen, J. W. Imaging and Mechanical Property Measurements of Kerogen via Nanoindentation Burruss. *Geochim. Cosmochim. Acta* **2004**, *68*, 4113−4119.

(10) Ahmadov, R. S. O.; Mavko, G.; Zoback, M.; Mukerji, T. *Microtextural, Elastic and Transport Properties of Source Rocks*; Stanford University, 2011.

(11) Ahmadov, R.; Vanorio, T.; Mavko, G. Confocal Laser Scanning and Atomic-Force Microscopy in Estimation of Elastic Properties of the Organic-Rich Bazhenov Formation. *Leading Edge* **2009**, *28*, 18−23.

(12) Kumar, V.; Sondergeld, C. H.; Rai, C. S. In *Nano to Macro Mechanical Characterization of Shale*, Proceedings - SPE Annual Technical Conference and Exhibition, 2012; pp 3421−3443.

(13) Eliyahu, M.; Emmanuel, S.; Day-Stirrat, R. J.; Macaulay, C. I. Mechanical Properties of Organic Matter in Shales Mapped at the Nanometer Scale. *Mar. Pet. Geol.* **2015**, *59*, 294−304.

(14) Valdes, C. C.; Heidari, Z.; Gonzalez, A. In *Quantifying the Impacts of Thermal Maturity on Elastic Properties of Kerogen*, SPWLA 58th Annual Logging Symposium, 2017.

(15) Zargari, S.; Prasad, M.; Mba, K. C.; Mattson, E. D. Organic Maturity, Elastic Properties, and Textural Characteristics of Self Resourcing Reservoirs. *Geophysics* **2013**, *78*, D223−D235.

(16) Burlingame, A. L.; Haug, P. A.; Schnoes, H. K.; Simoneit, B. R. Fatty Acids Derived from the Green River Formation Oil Shale by Extractions and Oxidations1)1This Review Represents Part XXVII in the Series High Resolution Mass Spectrometry in Molecular Structure Studies. For Part XXVI, See A.L. Burlingame and B.R. Simoneit, Nature, in Press.) — A Review. In *Advances in Organic Geochemistry 1968*; Elsevier B.V., 1969; pp 85−129.

(17) Yen, T. F. Structural Aspects of Organic Components in Oil Shales. In *Developments in Petroleum Science*; Elsevier B.V., 1976; Vol. 5.

(18) Siskin, M.; Scouten, C. G.; Rose, K. D.; Aczel, T.; Colgrove, S. G.; Pabst, R. E. Detailed Structural Characterization of the Organic Material in Rundle Ramsay Crossing and Green River Oil Shales. In *Composition, Geochemistry and Conversion of Oil Shales*; Springer, 1995; pp 143−158.

(19) Oka, M.; Hsueh-Chia, C.; Gavalas, G. R. Computer-Assisted Molecular Structure Construction for Coal-Derived Compounds. *Fuel* **1977**, *56*, 3−8.

(20) Ungerer, P.; Collell, J.; Yiannourakou, M. Molecular Modeling of the Volumetric and Thermodynamic Properties of Kerogen: Influence of Organic Type and Maturity. *Energy Fuels* **2015**, *29*, 91−105.

(21) Zhang, Z.; Jamili, A. In *Modeling the Kerogen 3D Molecular Structure*, Society of Petroleum Engineers - SPE/CSUR Unconventional Resources Conference, 2015; pp 1−14.

(22) Schuelke, J.; Yan, F.; Yan, F.; Han, D. H. In *Measurement of Elastic Properties of Kerogen*, Society of Exploration Geophysicists International Exposition and 83rd Annual Meeting, 2013; pp 2778−2782.

(23) Kashinath, A.; Szulczewski, M. L.; Dogru, A. H., *Modeling the Effect of Maturity on the Elastic Moduli of Kerogen Using Atomistic Simulations*, SPE/AAPG/SEG Unconventional Resources Technology Conference 2019, URTC 2019, 2019; pp 1−16.

(24) Bousige, C.; Ghimbeu, C. M.; Vix-guterl, C.; Pomerantz, A. E.; Suleimenova, A.; Vaughan, G.; Garbarino, G.; Feygenson, M.;

Wildgruber, C.; Ulm, F.; Pellenq, R. J.; Coasne, B. Realistic Molecular Model of Kerogen's Nanostructure. *Nat. Mater.* **2016**, *15*, 576−582.
(25) Nayebi, P.; Zaminpayma, E. A Molecular Dynamic Simulation Study of Mechanical Properties of Graphene-Polythiophene Composite with Reax Force Field. *Phys. Lett. A* **2016**, *380*, 628−633.
(26) Sheikhnejad, O. Molecular Dynamic Simulation of Carbon Nanotube Reinforced Nanocomposites: The Effect of Interface Interaction on Mechanical Properties. *MOJ Polym. Sci.* **2018**, *2*, 6−10.
(27) Chowdhury, S. C.; Haque, B. Z. Gama; Gillespie, J. W. Molecular Dynamics Simulations of the Structure and Mechanical Properties of Silica Glass Using ReaxFF. *J. Mater. Sci.* **2016**, *51*, 10139−10159.
(28) Buell, S.; Van Vliet, K. J.; Rutledge, G. C. Mechanical Properties of Glassy Polyethylene Nanofibers via Molecular Dynamics Simulations. *Macromolecules* **2009**, *42*, 4887−4895.
(29) Aljaberi, J.; Alafnan, S.; Glatz, G.; Sultan, A. S.; Afagwu, C. The Impact of Kerogen Tortuosity on Shale Permeability. *SPE J.* **2021**, *26*, 765−779.
(30) Alafnan, S. Petrophysics of Kerogens Based on Realistic Structures. *ACS Omega* **2021**, *6*, 9549−9558.
(31) Alafnan, S.; Falola, Y.; al Mansour, O.; AlSamadony, K.; Awotunde, A.; Aljawad, M. Enhanced Recovery from Organic-Rich Shales through Carbon Dioxide Injection: Molecular-Level Investigation. *Energy Fuels* **2020**, *34*, 16089−16098.
(32) Afagwu, C.; Al-Afnan, S.; Patil, S.; Aljaberi, J.; Mahmoud, M. A.; Li, J. The Impact of Pore Structure and Adsorption Behavior on Kerogen Tortuosity. *Fuel* **2021**, *303*, No. 121261.
(33) Alafnan, S.; Sultan, A. S.; Aljaberi, J. Molecular Fractionation in the Organic Materials of Source Rocks. *ACS Omega* **2020**, *5*, 18968−18974.
(34) Alafnan, S.; Solling, T.; Mahmoud, M. Effect of Kerogen Thermal Maturity on Methane Adsorption Capacity: A Molecular Modeling Approach. *Molecules* **2020**, *25*, No. 3764.
(35) Waldman, M.; Hagler, A. T. New Combining Rules for Rare Gas van Der Waals Parameters. *J. Comput. Chem.* **1993**, *14*, 1077−1084.
(36) Le Page, Y.; Saxe, P. Symmetry-General Least-Squares Extraction of Elastic Coefficients from Ab Initio Total Energy Calculations. *Phys. Rev. B* **2001**, *63*, No. 174103.
(37) Le Page, Y.; Saxe, P. Symmetry-General Least-Squares Extraction of Elastic Data for Strained Materials from Ab Initio Calculations of Stress. *Phys. Rev. B* **2002**, *65*, No. 104104.
(38) Jiang, D.; Wu, M.; Liu, D.; Li, F.; Chai, M.; Liu, S. Structural Stability, Electronic Structures, Mechanical Properties and Debye Temperature of Transition Metal Impurities in Tungsten: A First-Principles Study. *Metals* **2019**, *9*, No. 967.
(39) Hill, R. Elastic Properties of Reinforced Solids: Some Theoretical Principles. *J. Mech. Phys. Solids* **1963**, *11*, 357−372.
(40) Barber, C. B.; Dobkin, D. P.; Huhdanpaa, H. The Quickhull Algorithm for Convex Hulls. *ACM Trans. Math. Software* **1996**, *22*, 469−483.
(41) Xie, J.; Cao, J.; Schmitt, D. R.; Di, B.; Xiao, L.; Wang, X.; Wang, K.; Chen, Y. Effects of Kerogen Content on Elastic Properties-Based on Artificial Organic-Rich Shale (AORS). *J. Geophys. Res.: Solid Earth* **2019**, *124*, 12660−12678.
(42) Tang, X.; Jiang, Z.; Jiang, S.; Wang, P.; Xiang, C. Effect of Organic Matter and Maturity on Pore Size Distribution and Gas Storage Capacity in High-Mature to Post-Mature Shales. *Energy Fuels* **2016**, *30*, 8985−8996.
(43) Zhang, Y.; He, Z.; Jiang, S.; Lu, S.; Xiao, D.; Chen, G.; Zhao, J. Factors Affecting Shale Gas Accumulation in Overmature Shales Case Study from Lower Cambrian Shale in Western Sichuan Basin, South China. *Energy Fuels* **2018**, *32*, 3003−3012.
(44) Guo, X.; Huang, Z.; Ding, X.; Chen, J.; Chen, X.; Wang, R. Characterization of Continental Coal-Bearing Shale and Shale Gas Potential in Taibei Sag of the Turpan-Hami Basin, NW China. *Energy Fuels* **2018**, *32*, 9055−9069.
(45) Dasani, D.; Wang, Y.; Tsotsis, T. T.; Jessen, K. Laboratory-Scale Investigation of Sorption Kinetics of Methane/Ethane Mixtures in Shale. *Ind. Eng. Chem. Res.* **2017**, *56*, 9953−9963.

https://doi.org/10.1021/acsomega.2c02474
ACS Omega 2022, 7, 31801−31812